PAPER

Check for updates

Comparative analysis of the inhibitory effects of aloin on tyrosinase supported by Fe₃O₄@rGO: investigation of interaction mechanisms, inhibitory activity, and conformational changes†

Zhu Wang,[a] Lu Chen,[a] Jing Yuan,[b] Qiulan Zhang [ID] *[a] and Yongnian Ni [ID] [a]

Tyrosinase is a key enzyme that regulates the rate of melanin synthesis, thereby modulating both food browning and skin pigmentation. It has been found that aloin is an effective inhibitor of tyrosinase activity and Fe₃O₄@rGO has remarkable drug-loading capability. In this study, enzyme inhibition kinetics and multispectral techniques were employed to investigate the enzyme inhibitory effect of Fe₃O₄@rGO-aloin nanocomposites and evaluate their anti-browning effect and safety. The binding ability of tyrosinase and aloin was further enhanced by the addition of Fe₃O₄@rGO. The IC$_{50}$ value of Fe₃O₄@rGO-aloin against tyrosinase was determined to be $2.26 \pm 0.15 \times 10^{-5}$ mol L^{-1} with a typical anticompetitive inhibition. The findings suggest that Fe₃O₄@rGO-aloin exhibits a more potent inhibitory effect on tyrosinase compared to aloin. Furthermore, three-dimensional fluorescence, Fourier transform infrared and circular dichroism experiments demonstrated that aloin-loaded Fe₃O₄@rGO nanoparticles induce alterations in the secondary structure and conformation of tyrosinase. This indicates the potential of Fe₃O₄@rGO nanocomposites as candidates for the development of novel tyrosinase inhibitors for the treatment of hyperpigmentation disorders.

1 Introduction

Tyrosinase (TYR) is a pivotal enzyme containing copper metal that plays a crucial role in living organisms by facilitating the production of melanin, plant pigments, and thyroid hormones. Moreover, it catalyzes the conversion of hydroxy-containing L-tyrosine to levodopa and undergoes oxidation to form dopaquinone, ultimately leading to the synthesis of melanin.[1,2] If there is an elevated concentration or excessive activity of TYR within the body, it can result in the accumulation of melanin, thereby giving rise to various dermatological conditions such as hyperpigmentation, melasma, age spots, and even skin cancer.[3] Additionally, TYR plays a key role in cellular metabolism, and excessive enzymatic activity can give rise to metabolic disorders, thereby perturbing interconnected metabolic pathways and eliciting aberrant physiological responses within the organism.[4] *In vivo* and cell line experiments have been used to screen for TYR inhibitors.[5,6] Therefore, the inhibition of TYR catalytic activity and the development of highly potent and low-toxicity TYR inhibitors hold immense significance in addressing pigmentation disorders and restoring normal body metabolism. Because of kojic acid's widespread use in food preservation by effectively inhibiting TYR activity, many studies have investigated the inhibitory effects of kojic acid derivatives on TYR activity.[7] Peng *et al.* designed a series of gallic acid-benzylidenehydrazine hybrids and assessed their TYR inhibitory activity.[8] He *et al.* synthesized 15 novel kojic acid compounds bearing 1,2,4-triazine moieties and investigated their inhibitory activities and mechanisms on TYR.[9] Wang *et al.* synthesized 14 kojic acid 1,3,4-oxadiazole compounds and evaluated their TYR inhibitory activity.[10] Most of the kojic acid derivatives showed better anti-tyrosinase activity than kojic acid. In addition, hydroxypyranone thiocarbazone derivatives, 4H-chromene-3-carbonitrile derivatives and thiosemicarbazide derivatives also exhibited anti-tyrosinase activity.[11,12]

Meanwhile, natural compounds derived from plants, such as quercetagetin, verproside, polyphenols and so on, have also been recognized as promising sources of TYR inhibitors.[13,14] Aloin, derived from the aloe plant, has shown remarkable protective effects as an anti-tumor, anti-inflammatory,[15] cytoprotective, antioxidant, antibacterial,[16] anticancer,[17] antidiabetic, and osteogenic agent.[18] Previous work of our group confirmed that aloin has inhibitory effects on TYR.[19]

[a]School of Chemistry and Chemical Engineering, Nanchang University, Nanchang 330031, China. E-mail: qlzhang@ncu.edu.cn
[b]The Second Clinical Medical College, Nanchang University, Nanchang 330031, China

Due to their ability to interact at the molecular level, nano-scale particles have been used to improve the enzyme inhibitory activity of organic extracts.[20] Nevertheless, drug delivery systems often demonstrate a failure in the adhesion phase, resulting in the release of a high concentration of the therapeutic agent. This situation may lead to various health complications, including diminished effectiveness or liver damage. To solve these concerns, alternative methods for drug administration have been established. One notable pathway is the application of drugs on nanoporous carrier materials, such as activated carbon, graphene, and magnetic nanomaterials (Fe_3O_4). The drug encapsulation and transportation of graphene nanocomposites have been studied, as hydrophobic medications can be encapsulated onto graphene sheets through π–π stacking. Angelopoulou et al. created graphene oxide (GO)/poly(lactide)–poly(ethylene glycol) (PLA–PEG) nanocomposites containing paclitaxel, showing effective high loading capability, regulated release, and cytotoxic effects on A549 cancer cells.[21] Zhang et al. developed a PEG-modified nano-graphene oxide to transport paclitaxel and indocyanine green, demonstrating outstanding outcomes in fluorescence tagging and treatment efficacy.[22] Nanocarriers engineered to specifically bind natural drugs are employed to surmount the obstacles associated with the in vivo delivery and efficacy of small molecule drugs.[23] The US Food and Drug Administration has granted a license for the utilization of Fe_3O_4 as a drug carrier, owing to its exceptional biocompatibility, biodegradability, and minimal toxicity.[24] In the last ten years, GO modified with Fe_3O_4 nanoparticles has received considerable interest due to its potential uses in targeted drug delivery.[25] The broad P-conjugated network and the existence of various structural imperfections in the functional region of GO promote its modification with Fe_3O_4.[26] Owing to the ultra-fine size, biocompatibility, and magnetic behavior of Fe_3O_4 nanoparticles, these modified GO nanostructures are anticipated to effectively direct drug nanocarriers into specific cellular tissues via magnetic fields, thereby enhancing drug delivery efficiency.[27] In particular, when a focused magnetic field is utilized to aim at the cell site, the magnetic GO nanostructure can be guided to the cell via injection, which consequently facilitates the efficient accumulation of the drug at the targeted area.[28] Additionally, employing magnetic GO nanostructures can significantly improve drug availability, protect them from degradation prior to reaching targeted locations, and increase their concentration in specific cells by entering the bloodstream.[29] It has been proved that Fe_3O_4@rGO has good biological compatibility and safety in in vivo models.[30,31] Hence, this study presents the development of a composite drug delivery system based on graphene for magnetic targeting and drug delivery. Enzyme inhibition kinetics and multispectral techniques were employed to investigate the enzyme inhibitory effects of aloin-Fe_3O_4@rGO nanocomposites and evaluate their anti-browning effects and safety. The aim is to offer valuable insights for a deeper understanding of the loading dynamics of drug molecules and elucidate their binding mechanisms at the molecular level.

2 Materials and methods

2.1 Materials

TYR (1100 U mg^{-1}) and aloin (purity $\geq$ 95%) were purchased from Shanghai Yuanye Biotechnology Co. Ltd. L-Dopa (purity $\geq$ 99%) was obtained from McLean Biochemical Technology Co., Ltd. Stock solutions of TYR (8.32×10^{-5} mol L^{-1}), aloin (2.30×10^{-3} mol L^{-1}) and L-dopa (6.00×10^{-3} mol L^{-1}) were prepared using 0.05 mol L^{-1} sodium phosphate buffer saline (PBS, pH 6.8). 0.86 mg mL^{-1} Fe_3O_4@rGO suspension was prepared by dispersing 2.58 mg of Fe_3O_4@rGO black powder in 3.0 mL of double-distilled water. $FeCl_3$, $FeCl_2$, polyvinylpyrrolidone K30 (PVP), graphite powder and $NH_3 \cdot H_2O$ were all sourced from Sinophenol Chemical Reagent Co., Ltd (SCRC, Shanghai, China) and used without further purification. PBS (pH 6.8) was prepared by mixing disodium hydrogen phosphate (Shanghai McLin Biochemical Technology Co., Ltd) and sodium dihydrogen phosphate (Sinopharm Chemical Reagents Co., Ltd). The entire stock solution was stored at 5 °C, while fresh ultra-pure water was utilized throughout all experimental procedures.

2.2 Synthesis of Fe_3O_4@rGO

The synthesis of magnetic Fe_3O_4@rGO nanoparticles was achieved via the coprecipitation method.[32] First, a solution was prepared by dissolving $FeSO_4 \cdot 7H_2O$ (0.2780 g), $FeCl_3$ (0.3244 g) and PVP (10.0 mg) in 10.0 mL of ultra-pure water. Second, the solution was stirred at 80 °C for 30 min, followed by cooling it down to room temperature before adding ammonia water (5 mL) and GO solution (10 mL, with a concentration of 5 mg mL^{-1}). The resulting mixture was then subjected to ultrasound treatment at 25 °C for another 30 min. Finally, the mixture was transferred into a high-pressure reactor lined with a polytetrafluoroethylene container of capacity 100 ml, sealed tightly, and maintained at a temperature of 180 °C for a duration of 5 h and 30 min. After the autoclave had cooled down to room temperature, the product precipitated at the bottom of the container. The black product obtained was washed three times using ultra-pure water and ethanol solutions respectively before being dried in a vacuum drying oven at a temperature of 65 °C for a period of 12 h to yield Fe_3O_4@rGO powder. The Fe_3O_4@rGO nanomaterial was characterized using scanning electron microscopy (SEM), Fourier transform infrared spectroscopy (FT-IR) and X-ray diffraction (XRD). All experiments were performed at room temperature unless otherwise specified.

2.3 Ultraviolet-visible (UV-vis) experiments

An Agilent Cary 8454 UV-vis spectrometer equipped with a 1.0 cm cuvette (Thermo Fisher Technology Co., Shanghai) was utilized in this study. PBS (pH 6.8) was utilized as the blank solution. Three different combining sets of TYR, Fe_3O_4@rGO and aloin were added to 2.0 mL of PBS buffer solutions, respectively, and then three mixtures, TYR-Fe_3O_4@rGO, Fe_3O_4@rGO-aloin, and TYR-Fe_3O_4@rGO-aloin, were obtained.

2.4 Activity analysis of aloin against TYR

2.4.1 Assay for the activity of TYR. The TYR activity was determined by adapting and refining established methods from the literature, in accordance with rigorous scientific standards.[33] A series of L-dopa concentrations were prepared (1.25×10^{-4} mol L^{-1}, 2.50×10^{-4} mol L^{-1}, 5.00×10^{-4} mol L^{-1}, 1.00×10^{-3} mol L^{-1}, 2.00×10^{-3} mol L^{-1}, 3.00×10^{-3} mol L^{-1}, 4.00×10^{-3} mol L^{-1}, and 6.00×10^{-3} mol L^{-1}) along with a fixed concentration of TYR solution (2.08×10^{-7} mol L^{-1}) in a 2.0 mL volume. The absorbance of the reactants was measured at intervals of 10 s at 475 nm. The catalytic reaction of TYR follows the Michaelis–Menten kinetics (2.1):[34]

$$V = \frac{V_{max}S}{K_m + S} \tag{2.1}$$

The experimental data were subjected to statistical analysis using GraphPad Prism 8.0 software, and nonlinear fitting of TYR was performed based on eqn (2.1) to obtain the kinetic parameters K_m and V_{max} associated with the enzymatic reaction.

2.4.2 Effects of aloin and Fe$_3$O$_4$@rGO-aloin on TYR activity. The activity of TYR was quantified using the methodology previously established in our research.[35] The reaction system was supplemented with varying concentrations of aloin and Fe$_3$O$_4$@rGO-aloin solutions, while maintaining a fixed TYR concentration (8.32×10^{-7} mol L^{-1}). Subsequently, all samples were incubated at 30 °C in a water bath. After incubation, L-dopa was added (4.00×10^{-3} mol L^{-1}, substrate) and incubated for 5 min, and the absorbance was measured at 475 nm. The half maximal inhibitory concentration (IC$_{50}$) values of aloin and Fe$_3$O$_4$@rGO-aloin were determined based on the following conversion relationship in terms of enzyme activity:[36]

$$\text{Relative activity } (\%) = A_1/A_0 \times 100\% \tag{2.2}$$

where A_1 is the reaction rate of the system with aloin and Fe$_3$O$_4$@rGO-aloin and A_0 represents the reaction rate of the system without aloin and Fe$_3$O$_4$@rGO-aloin.

2.4.3 Inhibition kinetic analysis. The types of inhibition induced by polyphenols can be divided into competitive inhibition, non-competitive inhibition, anti-competitive inhibition and mixed inhibition.[37] According to the above experimental method for the determination of TYR activity, a series of aloin and Fe$_3$O$_4$@rGO-aloin with different concentrations were set up to determine the rate of L-dopa oxidation catalyzed by TYR, and the double reciprocal Lineweaver–Burk plot was drawn. The inhibition types of aloin and Fe$_3$O$_4$@rGO-aloin on TYR were determined, and their inhibition constants K_i were calculated. According to the Lineweaver–Burk equation, the inhibition mechanisms are analyzed as follows:[38]

$$\frac{1}{\nu} = \frac{K_m}{V_{max}}\left(1 + \frac{[I]}{K_i}\right)\frac{1}{[S]} + \frac{1}{V_{max}}\left(1 + \frac{[I]}{aK_i}\right) \tag{2.3}$$

Secondary plots were obtained from

$$\text{Slope} = \frac{K_m}{V_{max}} + \frac{K_m}{V_{max}}\frac{[I]}{K_i} \tag{2.4}$$

$$Y\text{-Intercept} = \frac{1}{V_{max}} + \frac{1}{aK_iV_{max}}[I] \tag{2.5}$$

where ν is the enzymatic reaction rate in the system; V_{max} denotes the maximum reaction rate; K_i is the dissociation constant of aloin and Fe$_3$O$_4$@rGO-aloin binding to the free enzyme; K_m denotes the Michaelis–Menten constant; [S] stands for the concentration of the substrate; and [I] and α represent the concentrations of the inhibitors and the apparent coefficient, respectively.

2.5 Fluorescence experiment

Fluorescence measurements were performed using an F-7100 fluorescence spectrophotometer (Hitachi, Japan) equipped with a 1.0 cm quartz colorimeter and an intelligent thermostatic water bath (Model ZC-10, Ningbo Tianhang Company, China). The scanning voltage was 450 V, the scanning speed was 1200 nm min^{-1}, and the excitation and emission silts were both 2.5 nm. The fluorescence spectra of the PBS buffer were collected at 280 nm excitation and then subtracted from the original fluorescence spectra of the sample. The internal filter and dilution effects were corrected before the binding and quenching data were analyzed.[39]

2.5.1 Fluorescence quenching experiment. In 2.0 mL of PBS buffer solution (pH 6.8), the concentration of TYR was fixed at 2.08×10^{-7} mol L^{-1}. Without and with Fe$_3$O$_4$@rGO (6.87×10^{-4} mg mL^{-1}), aloin was continuously added from 0–4.93×10^{-5} mol L^{-1} with intervals of 4.48×10^{-6} mol L^{-1}. The solution was incubated for 5 min, and then fluorescence quenching spectra were recorded three times at different temperatures (298 K, 301 K and 304 K).

2.5.2 Three-dimensional (3D) fluorescence assay. The 3D fluorescence spectra of TYR, TYR-Fe$_3$O$_4$@rGO and TYR-Fe$_3$O$_4$@rGO-aloin ($C_{TYR} = 7.18 \times 10^{-7}$ mol L^{-1}, $C_{Fe_3O_4@rGO} = 1.10 \times 10^{-3}$ mg mL^{-1}, and $C_{aloin} = 3.29 \times 10^{-6}$ mol L^{-1}) were recorded at a scanning speed of 2400 nm min^{-1}. The excitation wavelength is 200–400 nm (5.0 nm intervals), and the emission wavelength is 200–600 nm (1 nm intervals).

2.5.3 Synchronous fluorescence experiment. Synchronous fluorescence spectroscopic (SFS) analysis is based on previously reported methods.[40] The spectra were recorded at fixed C_{TYR} (5.72×10^{-7} mol L^{-1}) and $C_{Fe_3O_4@rGO}$ (9.17×10^{-4} mg mL^{-1}), and aloin was added 11 times from 0–10.18×10^{-5} mol L^{-1} at an interval of 9.26×10^{-6} mol L^{-1}. The fluorescence spectra at $\Delta\lambda$ ($\lambda_{em} - \lambda_{ex}$) values of 15 and 60 nm were measured.

2.6 Infrared experiment

FT-IR spectra were recorded on a Tensor 27 Fourier transform infrared spectrometer (Bruker, Germany) using the attenuated total reflectance (ATR) method with a resolution of 4 cm^{-1} and 60 scans. After the background spectra were subtracted, the FT-IR spectra of TYR, TYR-Fe$_3$O$_4$@rGO, and TYR-Fe$_3$O$_4$@rGO-aloin ($C_{TYR} = 3.83 \times 10^{-4}$ mol L^{-1}, $C_{Fe_3O_4@rGO} = 0.84$ mg mL^{-1} and $C_{aloin} = 3.30 \times 10^{-3}$ mol L^{-1}) were determined from 1800 to 1400 cm^{-1}.

2.7 Circular dichroism (CD) experiment

The CD spectra of pure TYR (C_{TYR} = 2.87 × 10^{-6} mol L^{-1}) and TYR solutions combined with Fe$_3$O$_4$@rGO ($C_{Fe_3O_4@rGO}$ = 0.60 mg mL^{-1}) and Fe$_3$O$_4$@rGO-aloin (C_{aloin} = 1.15 × 10^{-5} mol L^{-1}) were measured in the wavelength range of 190–250 nm using a CD spectrometer (Bio-Logic MOS 450, Claix, France) under a constant nitrogen atmosphere. The final spectra of all samples were obtained by subtracting the PBS spectrum. The secondary structure content of TYR was calculated using the online program (**https://dichroweb.cryst.bbk.ac.uk/html/process.shtml**).[41]

2.8 Time-resolved fluorescence assay

The time-resolved fluorescence decays of aloin-Fe$_3$O$_4$@rGO and aloin-Fe$_3$O$_4$@rGO-TYR were measured in a model FL920 CD fluorometer (Edinburgh Instruments, UK). The fluorescence decay monitored at 350 nm was obtained from 2 mL of aloin-Fe$_3$O$_4$@rGO solution (C_{aloin} = 3.14 × 10^{-5} mol L^{-1}, $C_{Fe_3O_4@rGO}$ = 7.31 × 10^{-4} mg mL^{-1}, pH 6.8) in the absence and in the presence of TYR (1.76 × 10^{-7} mol L^{-1}).

3. Results and discussion

3.1 Characterization of Fe$_3$O$_4$@rGO

The nanocomposites Fe$_3$O$_4$@rGO and GO were characterized using FT-IR, XRD, and SEM. The FT-IR spectrum (Fig. 1A) revealed three distinct characteristic peaks for Fe$_3$O$_4$@rGO at 562.5 cm^{-1}, 1653 cm^{-1}, and 3459 cm^{-1}, corresponding to the stretching vibrations of Fe–O, C=C, and O–H bonds. In addition, GO exhibited characteristic peaks at 1087 cm^{-1}, 1667 cm^{-1}, and 3468 cm^{-1}, related to the tensile vibrations of C–O, C=C, and O–H bonds respectively. In comparison with

the FT-IR spectrum of GO, the absence of an infrared peak at 1087 cm^{-1} in Fe$_3$O$_4$@rGO suggested the complete reduction of GO to reduced graphene oxide (rGO).[42] For Fe$_3$O$_4$@rGO-loaded aloin, the characteristic peaks at 553 cm^{-1}, 1235 cm^{-1}, 1608 cm^{-1}, and 3426 cm^{-1} correspond to the stretching vibrations of Fe–O, C–O, C=C, and O–H bonds, respectively. Compared with GO and Fe$_3$O$_4$@rGO, these characteristic peaks are broadened and shifted. Meanwhile, the characteristic peaks of aloin appear in the range of 1800–2500 cm^{-1}, indicating that aloin has been successfully loaded onto Fe$_3$O$_4$@rGO.[43,44] The XRD spectrum of Fe$_3$O$_4$@rGO exhibited a characteristic pure cubic spinel crystal structure (Fig. 1B). The diffraction pattern exhibited distinct peaks at approximately 30.3°, 35.8°, 43.0°, 53.6°, 57.0°, and 62.5°, which corresponded precisely to the (220), (311), (400), (422), (511), and (440) lattice diffractions of Fe$_3$O$_4$ (JCPDS card no.19-0629).[45] The folded shape of GO could be clearly observed in the SEM image shown in Fig. 1C. In the hydrothermal synthesis of Fe$_3$O$_4$@rGO (Fig. 1D), it was evident that spherical Fe$_3$O$_4$ particles were uniformly distributed on the surface of rGO, indicating the effective prevention of Fe$_3$O$_4$ nanoparticle aggregation by synthetic Fe$_3$O$_4$@rGO.[46] Moreover, as depicted in Fig. 1E, it was evident that the distribution of aloin on the surface of Fe$_3$O$_4$@rGO exhibited a remarkable uniformity.

3.2 UV-vis absorption used to study the complex formation

UV-vis absorption spectroscopy is a straightforward and efficient technique frequently employed for investigating the formation of ligand–protein complexes. As depicted in Fig. 2A, Fe$_3$O$_4$@rGO exhibited no discernible absorption peak, while the absorption peak intensity of the TYR-Fe$_3$O$_4$@rGO complex was obviously higher than that of TYR + Fe$_3$O$_4$@rGO (the combined absorption spectra of TYR and Fe$_3$O$_4$@rGO), indicating
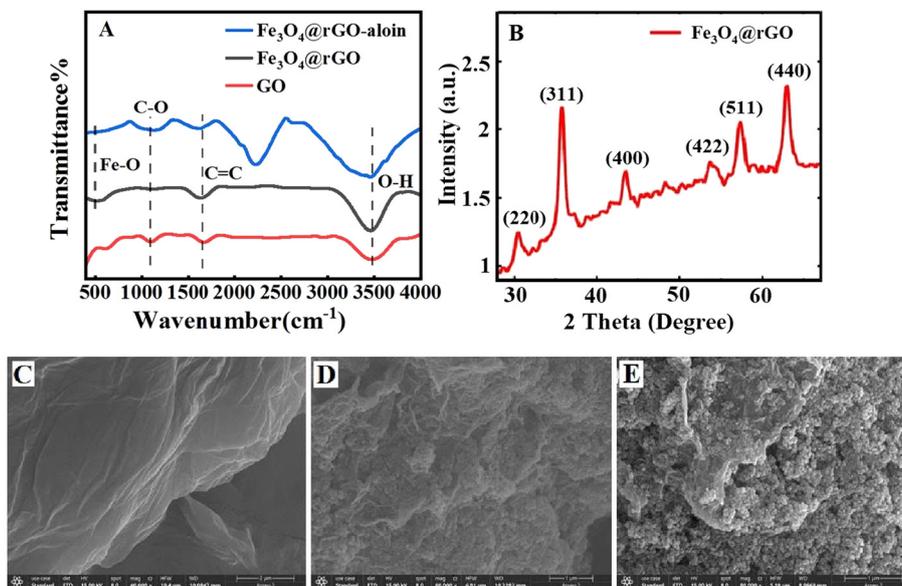
Fig. 1 (A) FT-IR spectra of Fe$_3$O$_4$@rGO and GO; (B) XRD spectra of Fe$_3$O$_4$@rGO; and SEM images of (C) GO; (D) Fe$_3$O$_4$@rGO; and (E) Fe$_3$O$_4$@rGO-aloin.
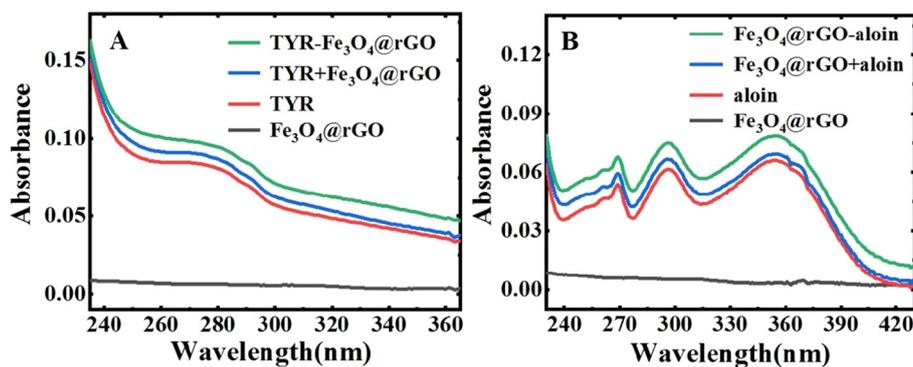
Fig. 2 The UV-vis spectra of TYR-Fe$_3$O$_4$@rGO (A) and Fe$_3$O$_4$@rGO-aloin (B) (C_{TYR} = 2.34 × 10^{-7} mol L^{-1}, C_{aloin} = 3.89 × 10^{-6} mol L^{-1}, and $C_{Fe_3O_4@rGO}$ = 5.83 × 10^{-4} mg mL^{-1}).

that the interaction between TYR and Fe$_3$O$_4$@rGO affects the absorption characteristics of TYR.[47] This suggests that the fixation of TYR onto the surface of Fe$_3$O$_4$@rGO may be attributed to the substantial specific surface area of the Fe$_3$O$_4$@rGO nanomaterial. The spectra of aloin with and without Fe$_3$O$_4$@rGO were compared, revealing an increase in the UV absorption peak intensity of aloin. Additionally, a slight blue shift was observed at 262 nm, 293 nm, and 351 nm (approximately 2 nm difference: from 262/293/351 nm to 260/291/349 nm) (Fig. 2B). Moreover, the absorption peak intensity of Fe$_3$O$_4$@rGO-aloin surpassed that of Fe$_3$O$_4$@rGO + aloin, implying that the incorporation of aloin onto Fe$_3$O$_4$@rGO involved more than mere adsorption. The results indicated that the formation of the Fe$_3$O$_4$@rGO-aloin complex was facilitated by the hydrogen bonding between the hydroxyl group of aloin and the surface of Fe$_3$O$_4$@rGO. According to the formula,[48] the drug-loading capacity (DL) and encapsulation efficiency (EE) of Fe$_3$O$_4$@rGO with aloin were 30.80% and 12.64%, respectively (ESI and Fig. S1†).

3.3 Activity analysis of aloin against TYR

3.3.1 Determination of TYR activity. The horizontal axis in Fig. 3A represented the varying concentrations of the substrate L-dopa, while the vertical axis corresponded to the maximum reaction rate. The Michaelis constant (K_m) value of the catalytic substrate L-dopa for the TYR reaction was determined to be 4.70 ± 2.4 × 10^{-4} mol L^{-1} using the Michaelis–Menten equation. The maximum reaction rate (V_{max}) was determined to be 2.59 ± 0.30 × 10^{-6} mol L^{-1} s^{-1}.

3.3.2 Inhibitory effects of aloin and Fe$_3$O$_4$@rGO-aloin on TYR activity. Aloin and Fe$_3$O$_4$@rGO-aloin exhibited concentration-dependent inhibitory activity against TYR. As illustrated in Fig. 3B, different concentrations of aloin and Fe$_3$O$_4$@rGO-aloin were added to a 2 mL reaction system containing L-dopa as the substrate to investigate their impact on TYR activity. The results demonstrated a negative correlation between the relative activity of TYR and the concentration of aloin and Fe$_3$O$_4$@rGO-aloin, suggesting that both aloin and Fe$_3$O$_4$@rGO-aloin exerted inhibitory effects on TYR activity. The IC$_{50}$ values of aloin and Fe$_3$O$_4$@rGO-aloin for TYR can be determined from Fig. 3B as 4.04 ± 0.53 × 10^{-5} mol L^{-1} and 2.26 ± 0.15 × 10^{-5} mol L^{-1}, respect-

ively. The IC$_{50}$ value of Fe$_3$O$_4$@rGO-aloin for TYR is superior to those listed in Table S1,† suggesting that Fe$_3$O$_4$@rGO-aloin has the potential to be used as a TYR inhibitor.

3.3.3 Kinetic type of inhibition. By analyzing the Lineweaver–Burk plot, we could discern the nature of inhibition in a more intuitive and scientifically rigorous manner. When the intersection of all lines coincides with the X-axis, it indicates non-competitive inhibition. Conversely, when the intersection of all lines aligns with the Y-axis, it signifies competitive inhibition. In cases where the intersection of all lines falls within the second and third quadrants, mixed suppression is observed. Lastly, if all lines are parallel without any intersections, this corresponds to anti-competitive suppression.[49]

The inhibition types of aloin and Fe$_3$O$_4$@rGO-aloin on TYR were analyzed using the Lineweaver–Burk double reciprocal diagram (Fig. 3C and D). The Lineweaver–Burk plot revealed that the lines intersected in the second quadrant with varying slopes, and as the aloin concentration increased, the plots exhibited steeper slopes, indicating a decreasing trend in maximum velocity (V_{max}). The results suggested a mixed inhibitory effect of aloin on TYR activity. Furthermore, the Lineweaver–Burk plot of TYR for Fe$_3$O$_4$@rGO-aloin exhibited parallelism, indicating typical anti-competitive inhibition. Compared with competitive and non-competitive inhibition, an inhibitor with anti-competitive inhibition does not directly bind to the enzyme but binds to the enzyme–substrate complex to form an enzyme–substrate–inhibitor complex (the complex cannot produce oxidative products), thereby affecting the progress of enzyme catalysis.[50] Since aloin is loaded on Fe$_3$O$_4$@rGO, it changes the inhibition of TYR by the combined effect of Fe$_3$O$_4$@rGO-aloin. The values of K_i and K_{is} (equilibrium constant for the binding of aloin to TYR–substrate complex, $K_{is} = \alpha K_i$), which are crucial kinetic parameters for inhibition, can be determined by analyzing the slope (Fig. S2A†) and Y-intercept (Fig. S2B and S2C†) of the aloin/Fe$_3$O$_4$@rGO-aloin concentration. The K_i and K_{is} values for aloin inhibition of TYR were determined to be 3.02 × 10^{-5} mol L^{-1} and 5.54 × 10^{-5} mol L^{-1}, respectively. However, as depicted in Fig. 3D, both the K_m value and V_{max} exhibited a decrease with increasing Fe$_3$O$_4$@rGO-aloin concentration. This indi-
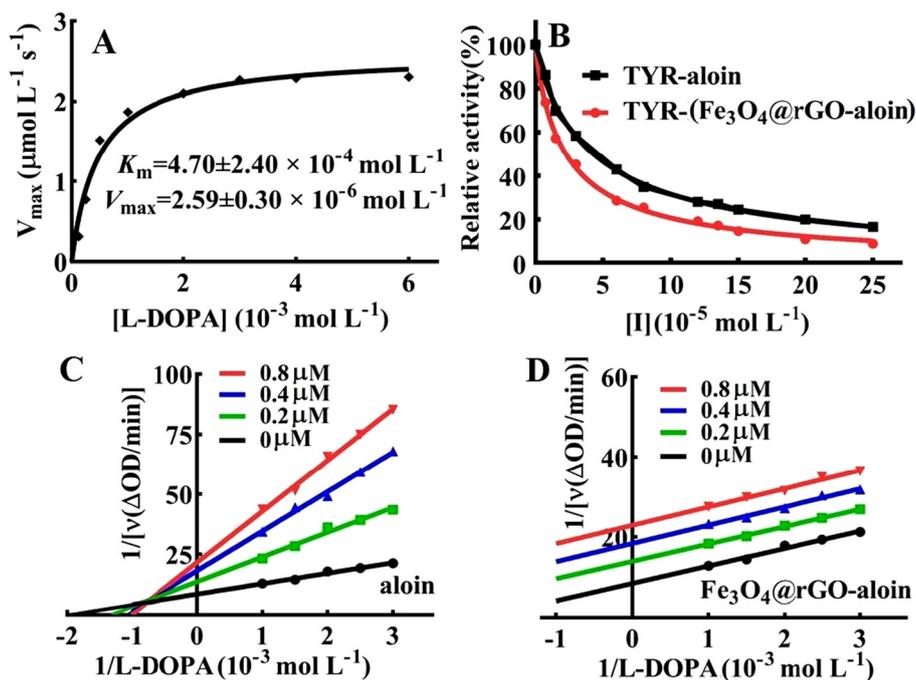
Fig. 3 (A) Catalytic reaction of TYR with the substrate L-dopa; (B) Effect of aloin and Fe_3O_4@rGO-aloin on TYR activity; (C) Lineweaver–Burk diagram of aloin inhibition of TYR; and (D) Lineweaver–Burk diagram of Fe_3O_4@rGO-aloin inhibition of TYR; C_{aloin} = 0.0, 2.0, 4.0 and 8.0 × 10^{-5}; $C_{Fe_3O_4@rGO}$ = 4.27 × 10^{-4} mg mL^{-1}.

cates that the presence of Fe_3O_4@rGO changes the inhibition mode of aloin on TYR from the original mixed-type to uncompetitive inhibition. This suggests that Fe_3O_4@rGO-aloin cannot directly bind to free TYR, but must first bind to the TYR–substrate complex. Meanwhile, it indicates that Fe_3O_4@rGO-aloin can bind at a non-active site of TYR. Such binding may alter the enzyme's conformation, thereby further affecting its catalytic activity.[51] The inhibition constants, $K_{i\ aloin}$ and $K_{i\ Fe_3O_4@rGO-aloin}$, were determined to be 3.02 × 10^{-5} mol L^{-1} and 1.52 × 10^{-5} mol L^{-1}, respectively. It is noteworthy that $K_{i\ aloin}$ > $K_{i\ Fe_3O_4@rGO-aloin}$, indicating a stronger inhibitory effect of Fe_3O_4@rGO-aloin compared to aloin. The anti-browning properties of aloin and Fe_3O_4@rGO-aloin in freshly cut apples were assessed. As depicted in Fig. S3,† the control group had almost no anti-browning effect on the apple slices, while the Fe_3O_4@rGO-aloin group exhibited a more significant anti-browning effect than the aloin group. Moreover, the photographs also indicated that Fe_3O_4@rGO-aloin could prevent the apple slices from noticeable browning when stored at room temperature for up to 40 hours. This finding substantiates the preeminence of Fe_3O_4@rGO nanocomposites in the advancement of prospective whitening therapeutics or targeted drug delivery for skin lightening.[52]

3.4 Study of fluorescence quenching

Fluorescence spectroscopy analyzes the excitation reaction, energy transfer, and collisional quenching to study the interaction between proteins and ligands. In order to investigate the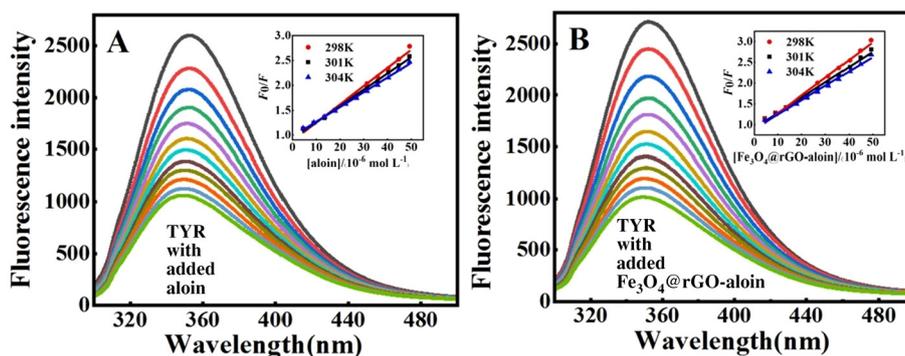 interaction between TYR and aloin in the presence or absence of Fe_3O_4@rGO, fluorescence quenching experiments were employed as an effective method. The fluorescence intensity of TYR exhibited a prominent peak at approximately 348 nm (with an excitation wavelength of 280 nm), whereas both aloin and Fe_3O_4@rGO-aloin exhibited negligible fluorescence peaks (Fig. 4). With the increase of aloin/Fe_3O_4@rGO-aloin in the TYR solution, the fluorescence signal of TYR diminishes gradually, while both aloin and Fe_3O_4@rGO-aloin induce a slight blue shift in the emission peaks of TYR. The observed blue shift indicates that aloin/Fe_3O_4@rGO-aloin induces specific structural modifications in TYR, resulting in the encapsulation of its hydrophobic residues within a hydrophobic environment rather than their exposure.[53] Meanwhile, the fluorescence intensity of TYR gradually diminished, indicating that both aloin and Fe_3O_4@rGO-aloin interacted with TYR to quench its fluorescence. In order to further investigate the intrinsic fluorescence quenching mechanism of TYR by aloin/Fe_3O_4@rGO-aloin, the well-established Stern–Volmer and double log equations (eqn (3.1) and (3.2)) were employed. The corresponding experimental data are summarized in Table 1.[54]

$$F_0/F = 1 + K_{sv}[Q] = 1 + K_q\tau_0 \quad (3.1)$$

$$\log\left(\frac{F_0 - F}{F}\right) = \log K_b + n\log[Q] \quad (3.2)$$

Here, F_0 and F denote the fluorescence intensity of TYR prior to and subsequent to the addition of aloin/Fe_3O_4@rGO-aloin, respectively. The Stern–Volmer quenching constant, K_{sv}, is denoted as a measure of quenching efficiency, while the bio-

Fig. 4 (A) Fluorescence quenching spectra of the interaction between aloin and TYR; (B) fluorescence quenching spectra of aloin and TYR in the presence of Fe_3O_4@rGO. $C_{TYR} = 2.08 \times 10^{-7}$ mol L^{-1}, $C_{Fe_3O_4@rGO} = 6.87 \times 10^{-4}$ mg mL^{-1}, and $C_{aloin} = 0-49.28 \times 10^{-6}$ mol L^{-1} (with an interval of 4.48×10^{-6} mol L^{-1}, 12 times). The inset figures in Fig. 4 is the quenching effect graphs of the Stern–Volmer equation.

Table 1 The binding constants and thermodynamic parameters of TYR-aloin and TYR-(Fe_3O_4@rGO-aloin)

T (K)	K_{sv} ($\times 10^4$ L mol^{-1})	R^2	n	K_b ($\times 10^4$ L mol^{-1})	$\Delta G°$ (kJ mol^{-1})	$\Delta H°$ (kJ mol^{-1})	$\Delta S°$ (J mol^{-1} K^{-1})
TYR-aloin							
298	3.60 ± 0.10	0.9933	0.98	2.35	−25.01	182.57	696.56
301	3.21 ± 0.06	0.9969	1.06	5.35	−27.10		
304	2.91 ± 0.05	0.9971	1.12	10.10	−29.19		
TYR-(Fe_3O_4@rGO-aloin)							
298	4.27 ± 0.14	0.9905	1.14	7.72	−27.88	42.20	235.15
301	3.67 ± 0.12	0.9907	1.04	9.09	−28.59		
304	3.44 ± 0.01	0.9926	1.12	10.80	−29.29		

molecule quenching rate constant, K_q ($K_q = K_{sv}/\tau_0$), represents the rate at which the fluorophore is deactivated by the biomolecule. Herein, τ_0 refers to the average lifetime of the fluorophore in the absence of a quencher and is equal to 10^{-8} s. Additionally, [Q] denotes the concentration of aloin/Fe_3O_4@rGO-aloin. The binding constant, K_b, and the number of binding sites, n, are essential parameters in characterizing the fluorescence quenching process. This mechanism can be categorized into dynamic quenching and static quenching. Dynamic quenching arises from collisions between the fluorophore and the quencher molecules, while static quenching predominantly results from the formation of non-fluorescent ground-state complexes between the fluorophore and the quencher. Dynamic quenching and static quenching can be distinguished by different dependences on the temperature of quenching constants or viscosity. K_{sv} is considered to be a method for the fluorescence quenching efficiency of quenchers. When K_{sv} increases with temperature, it exhibits a dynamic quenching mechanism, wherein higher temperatures lead to accelerated diffusion rates and collision-induced quenching.[55] In contrast, as the temperature increases, K_{sv} exhibits static quenching behavior, leading to the formation of a non-fluorescent ground-state complex through binding between the quenching molecule and the protein. According to the data obtained in Table 1, the K_{sv} values between aloin/Fe_3O_4@rGO-aloin and TYR decreased with increasing temperature (from $3.60 \pm 0.10 \times 10^4$ L mol^{-1} to $2.91 \pm 0.05 \times 10^4$ L mol^{-1} and $4.27 \pm 0.14 \times 10^4$ L mol^{-1} to $3.44 \pm 0.01 \times 10^4$ L

mol^{-1}, respectively), which means that the quenching mechanism of the two systems is static quenching, leading to the formation of ground-state complexes. In the warmed state, the static quenching increases the molecular thermal motion of the small molecules and proteins forming the ground state complex, which can effectively inhibit the activity of TYR.[56] Additionally, it is noteworthy that the K_{sv} value of TYR-Fe_3O_4@rGO-aloin surpasses that of TYR-aloin at identical temperatures, thereby indicating a superior fluorescence quenching effect of Fe_3O_4@rGO-aloin on TYR compared to single aloin. The K_b values of aloin and Fe_3O_4@rGO-aloin were approximately 10^4 L mol^{-1}, indicating a moderate binding affinity for TYR in both aloin and Fe_3O_4@rGO-aloin. Additionally, the n values exhibited proximity to 1, indicating the presence of a solitary binding site on TYR.[57] In addition, the K_b values increased with temperature and were higher for Fe_3O_4@rGO-aloin compared to aloin at the same temperature, indicating a stronger binding affinity between Fe_3O_4@rGO-aloin and TYR. Furthermore, the stability of the TYR-Fe_3O_4@rGO-aloin complex also increased with temperature. The fixation of aloin onto the surface of the Fe_3O_4@rGO nanomaterial potentially enhances the likelihood of contact between TYR and aloin, leading to an elevation in the binding constant.[58]

In general, small molecules bound to biological macromolecules are subject to four interaction forces: hydrophobic interactions, electrostatic forces, hydrogen bonding, and van der Waals forces.[59] The type of force can be determined by analyzing the positive and negative enthalpy change ($\Delta H°$) and

entropy change (ΔS°) in thermodynamic parameters. Therefore, the primary driving force behind the synergistic effect of aloin or Fe$_3$O$_4$@rGO-aloin in combination with TYR can be characterized by the thermodynamic parameters derived from the well-established van't Hoff equations:

$$\ln K_b = -\Delta H^\circ/RT + \Delta S^\circ/R \qquad (3.3)$$

$$\Delta G^\circ = \Delta H^\circ - T\Delta S^\circ \qquad (3.4)$$

where ΔH°, ΔS°, ΔG°, R and T stand for enthalpy change, entropy change, free energy change, gas constant (8.314 J mol^{-1} K^{-1}) and temperature, respectively. The negative values of ΔG° indicated that aloin and Fe$_3$O$_4$@rGO-aloin interactions with TYR were both spontaneous processes, and the positive values of ΔS° indicated that the aloin-TYR/Fe$_3$O$_4$@rGO-aloin-TYR systems become more disordered. Moreover, the positive ΔH° and ΔS° values indicated that hydrophobic action played a major role in the formation and stabilization of the aloin-TYR/Fe$_3$O$_4$@rGO-aloin-TYR complex,[60] and hydrogen bonds may also be involved in the binding due to its polyhydroxyl structure.

3.5 Excitation–emission matrix analysis

The 3D fluorescence spectrum enables the comprehensive visualization of chromophore fluorescence information, thereby enhancing the scientific investigation of protein conformational changes. The excitation–emission matrix fluorescence spectra of TYR exhibited variations upon interaction with Fe$_3$O$_4$@rGO-aloin, indicating the presence of an interaction between Fe$_3$O$_4$@rGO-aloin and TYR (Fig. 5). Peaks 1 and 2 were Rayleigh scattering peaks ($\lambda_{em} = \lambda_{ex}$) and second-order scattering peaks ($\lambda_{em} = 2\lambda_{ex}$), respectively. Peak a mainly represented the fluorescence properties of the polypeptide backbone. Peak b essentially stood for the spectral behavior of tryptophan and tyrosine residues.[61]

After the introduction of Fe$_3$O$_4$@rGO into TYR, slight shifts in the positions of peak a and peak b were observed (Table 2). The fluorescence intensities of peak a and peak b exhibited minimal changes, with decreases of 13.74% and 7.48%, respectively. This suggests that the conformational change of TYR was minimally affected by Fe$_3$O$_4$@rGO, indicating the excellent biocompatibility and low toxicity of Fe$_3$O$_4$@rGO as a potential drug carrier.[62] However, upon the addition of Fe$_3$O$_4$@rGO-aloin to the TYR solution, peak a exhibited a decrease in intensity from 1093 to 688.3 along with a shift in its position. This observation signifies perturbation of the peptide backbone and alteration of the microenvironment resulting from binding.[63] Additionally, when combined with Fe$_3$O$_4$@rGO-aloin, the intensity of peak b decreases from 660.5 to 489.8, and the Stokes shift varies slightly, suggesting that Fe$_3$O$_4$@rGO-aloin influences the secondary structure of TYR. Therefore, it can be postulated that the interaction with Fe$_3$O$_4$@rGO-aloin perturbed the polypeptide backbone, resulting in a more relaxed conformation.[64]

3.6 Conformational alterations of TYR in its binding with aloin in the presence and absence of Fe$_3$O$_4$@rGO

SFS was employed to characterize the impacts of Fe$_3$O$_4$@rGO-aloin on the hydrophobicity and polarity of tyrosine (Tyr) and tryptophan (Trp) residues within TYR. The fluorescence quenching of TYR by Fe$_3$O$_4$@rGO-aloin revealed a significant impact of Fe$_3$O$_4$@rGO-aloin on the microenvironment surrounding TYR. The SFS at $\Delta\lambda$ = 15 nm and 60 nm were utilized to investigate the polarity changes in the microenvironments of Tyr and Trp residues, respectively (Fig. 6A and B).[65] The fluorescence intensities of Tyr and Trp gradually diminished with the continuous addition of Fe$_3$O$_4$@rGO-aloin, indicating their interaction with Fe$_3$O$_4$@rGO-aloin and the subsequent quenching of internal fluorescence. Simultaneously, the

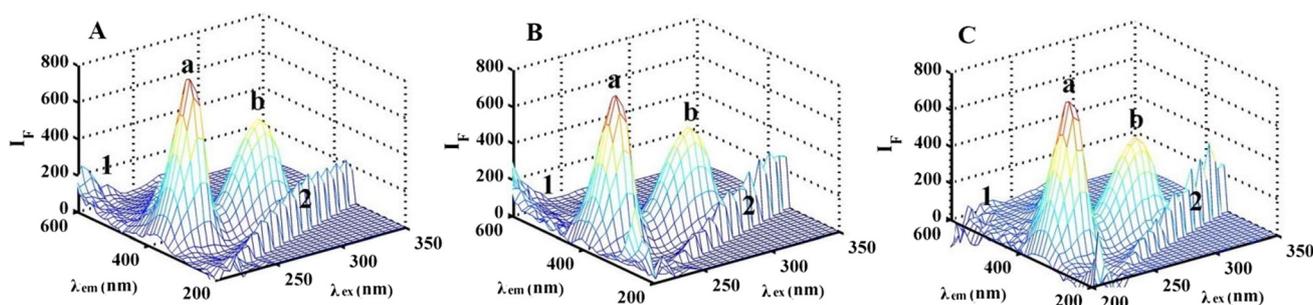**Fig. 5** Three-dimensional fluorescence spectra. (A) TYR; (B) TYR-Fe$_3$O$_4$@rGO; and (C) TYR-(Fe$_3$O$_4$@rGO-aloin). C_{TYR} = 7.18 × 10^{-7} mol L^{-1}, C_{aloin} = 3.29 × 10^{-6} mol L^{-1} and $C_{Fe_3O_4@rGO}$ = 1.10 × 10^{-3} mg mL^{-1}.

Table 2 Analysis of three-dimensional spectral data of TYR, TYR-Fe$_3$O$_4$@rGO and TYR-(Fe$_3$O$_4$@rGO-aloin)

Compounds	Peak a	$\Delta\lambda$	Intensity F	Peak b	$\Delta\lambda$	Intensity F
TYR	225/354	129	1093	280/352	72	660.5
TYR-Fe$_3$O$_4$@rGO	225/351	126	942.8	280/353	73	611.1
TYR-(Fe$_3$O$_4$@rGO-aloin)	225/350	125	688.3	280/351	71	489.8
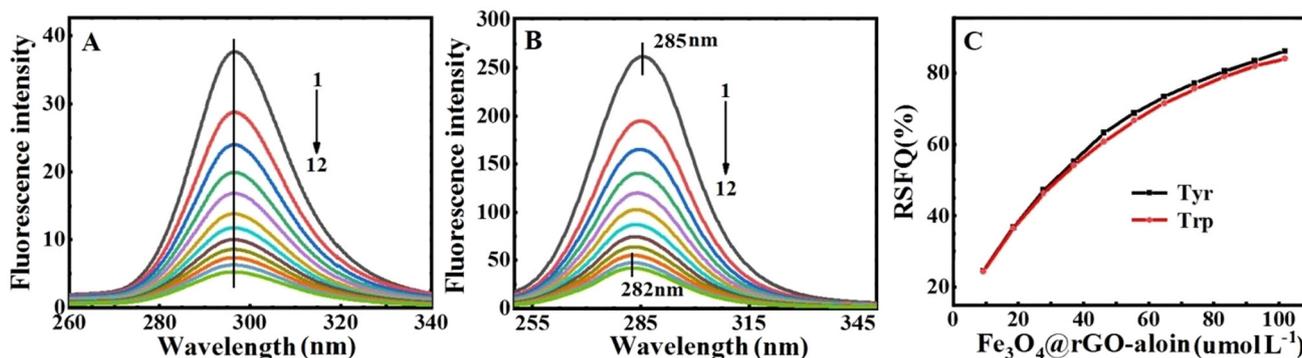
Fig. 6 (A) ($\Delta\lambda = 15$ nm) and (B) ($\Delta\lambda = 60$ nm) show synchronous fluorescence spectra of TYR and aloin in the presence of $Fe_3O_4@rGO$. $C_{TYR} = 5.72 \times 10^{-7}$ mol L^{-1}, $C_{Fe_3O_4@rGO} = 9.17 \times 10^{-4}$ mg mL^{-1}, and $C_{aloin} = 0-10.18 \times 10^{-5}$ mol L^{-1} (with an interval of 9.26×10^{-6} mol L^{-1}, 11 times) corresponding to curves $1 \rightarrow 12$, respectively. (C) Comparative evaluation of the impact of $Fe_3O_4@rGO$-aloin on the synchronous fluorescence quenching ratios (RSFQ) of TYR.

addition of $Fe_3O_4@rGO$-aloin did not lead to the shift of the fluorescence peak of the Tyr residue; however, it resulted in a blue shift of the fluorescence peak of the Trp residue from 285 nm to 282 nm (~3 nm). This observation suggested that $Fe_3O_4@rGO$-aloin did not have a noticeable effect on the surroundings of Tyr residues, but it could potentially lead to changes in the environment surrounding Trp residues. Therefore, these findings qualitatively emphasize the impact of the $Fe_3O_4@rGO$-aloin-TYR interaction on the conformation and microenvironment of TYR. Moreover, the values of the ratio of synchronous fluorescence quenching (RSFQ), calculated by virtue of the equation RSFQ = $1 - F/F_0$, were used to compare the contribution of Tyr and Trp residues in fluorescence quenching (Fig. 6C). The results revealed that the RSFQ values at $\Delta\lambda = 15$ nm and 60 nm nearly overlap for $Fe_3O_4@rGO$-aloin, signifying that the Tyr and Trp residues contribute approximately equal amounts to TYR fluorescence quenching.[66]

FT-IR was used to study the secondary structure of TYR. There were two typical amide bands in the infrared spectrum of proteins, mainly amide I band ($1700-1600$ cm^{-1}) and amide II band ($1600-1500$ cm^{-1}). The former mainly reflected the C=O stretching property, while the latter mainly reflected the C–N stretching and N–H bending. This was a prominent feature of protein groups in Fourier transform infrared spectroscopy, which was of great significance for determining the composition and conformational change of the protein secondary structure. Since the amide I band ($1600-1700$ cm^{-1}) played a major role in the secondary structural changes of proteins, the amide I band was more frequently used to evaluate the secondary structural changes of proteins. With the addition of $Fe_3O_4@rGO$, the characteristic absorption peaks of the amide I and amide II bands of TYR did not shift significantly (Fig. 7A). However, with the addition of $Fe_3O_4@rGO$-aloin, the characteristic absorption peaks of amide I and amide II bands of TYR shifted to different degrees (the amide I band shifted from 1645 cm^{-1} to 1632 cm^{-1} and the amide II band moved from 1533 cm^{-1} to 1537 cm^{-1}). The results suggested that $Fe_3O_4@rGO$ had little effect on the structure of

TYR, while $Fe_3O_4@rGO$-aloin had a certain extent effect on the changes in the functional groups (C=O and C–N) of the structure of TYR, which changed the conformation of TYR and affected the catalytic activity of TYR.

To determine the change in the secondary structure, the curve-fittings were used to analyze the amide I band. The amide I band can be divided into five band ranges and the spectral ranges of $1660-1650$ cm^{-1}, $1680-1660$ cm^{-1}, $1692-1680$ cm^{-1}, $1648-1638$ cm^{-1} and $1637-1610$ cm^{-1} were due to α-helix, β-turn, β-antiparallel, random coil and β-sheet structure, respectively. As shown in Fig. 7B, the free TYR contained 26.97% α-helix, 23.59% β-turn, 9.59% β-antiparallel, 22.91% random coil and 16.48% β-sheet. The conformation of TYR did not change much with the addition of $Fe_3O_4@rGO$ (Fig. 7C). With the addition of [$Fe_3O_4@rGO$-aloin]:[TYR] (from 0:1 to 8:1), a decreasing tendency of the contents of α-helix, random coil, and β-turn tended to decrease (from 26.97% to 14.55%, from 22.91% to 16.46% and from 23.59% to 14.41%, respectively), while the contents of β-sheet and β-antiparallel tended to increase (from 16.48% to 43.35% and from 9.59% to 11.23%) (Fig. 7D). These results imply that the interaction between $Fe_3O_4@rGO$-aloin and TYR modifies the polypeptide chain and eventually causes a transformation in the conformation of TYR. Consequently, it is believed that $Fe_3O_4@rGO$-aloin exhibits anti-tyrosinase activity by interacting with TYR and disrupting the structure.

3.7 CD spectroscopy

To investigate the effect of aloin on the secondary structure of TYR, the CD spectra (190–240 nm) of TYR were measured in the presence and absence of $Fe_3O_4@rGO$. As shown in Fig. 8, the CD intensity of the characteristic peaks of TYR changed little with the addition of $Fe_3O_4@rGO$. However, the CD intensity of the characteristic peaks of TYR increased with the addition of $Fe_3O_4@rGO$-aloin. This indicates that $Fe_3O_4@rGO$ has little effect on the secondary structure of TYR, while $Fe_3O_4@rGO$-aloin, due to its interaction with TYR, changes the secondary structure of TYR. As shown in Table 3, free TYR con-
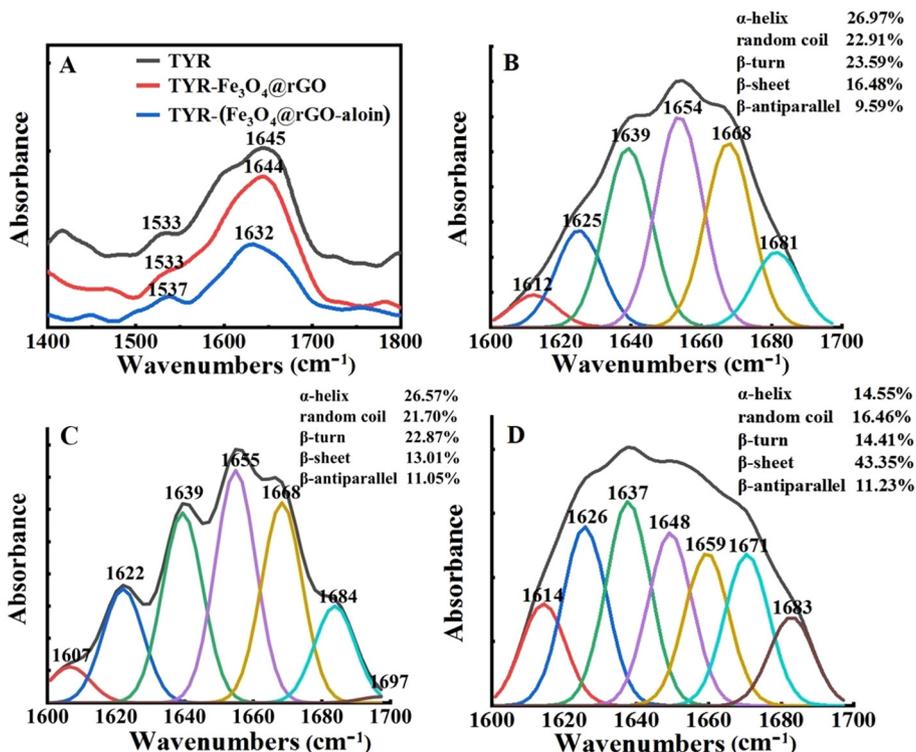
Fig. 7 (A) Infrared spectra of free TYR, TYR-Fe$_3$O$_4$@rGO and TYR-Fe$_3$O$_4$@rGO-aloin (C_{TYR} = 3.83 × 10^{-4} mol L^{-1}, $C_{Fe_3O_4@rGO}$ = 0.84 mg mL^{-1}, and C_{aloin} = 3.30 × 10^{-3} mol L^{-1}). (B, C and D) show the curve-fitted amide I region of free TYR, TYR-Fe$_3$O$_4$@rGO, and TYR-(Fe$_3$O$_4$@rGO-aloin), respectively.
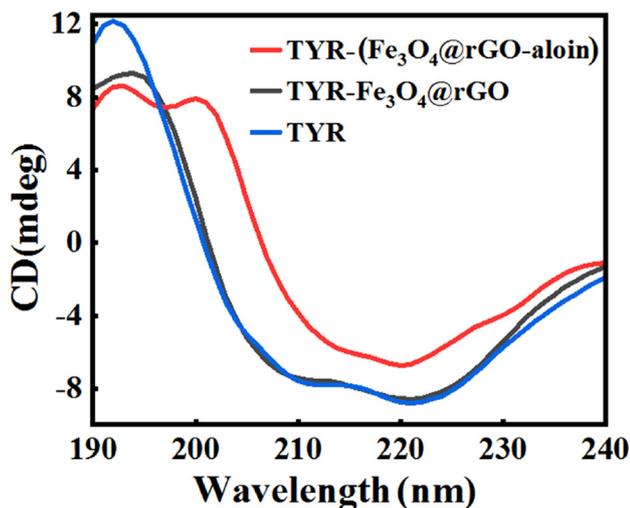
Fig. 8 CD spectra of the interaction between Fe$_3$O$_4$@rGO or Fe$_3$O$_4$@rGO-aloin and TYR at 298 K (C_{TYR} = 2.87 × 10^{-6} mol L^{-1}, $C_{Fe_3O_4@rGO}$ = 0.60 mg mL^{-1}, and C_{aloin} = 1.15 × 10^{-5} mol L^{-1}).

Table 3 The secondary structure content of TYR in the presence and absence of Fe$_3$O$_4$@rGO/Fe$_3$O$_4$@rGO-aloin

Compounds	α-Helix (%)	β-Sheet (%)	β-Turn (%)	Random coil (%)
TYR	22.3	26.9	29.7	21.1
TYR-Fe$_3$O$_4$@rGO	21.6	25.3	32.6	20.5
TYR-Fe$_3$O$_4$@rGO-aloin	12.8	49.5	20.2	17.5

from 21.1% to 17.5%, and from 29.7% to 20.2%, respectively), while the content of β-sheet shows an upward trend (from 26.9% to 49.5%). These results indicate that after binding with Fe$_3$O$_4$@rGO-aloin, the hydrogen bond network between the helical structures of TYR is disrupted, leading to a more relaxed conformation of TYR. It was reported that the content of α-helix was inversely proportional to TYR activity, the greater the conformational change induced by the inhibitor, the stronger the inhibitory ability.[67] Fe$_3$O$_4$@rGO-aloin inhibits TYR activity by altering its spatial structure and causing it to lose its normal physiological function.

3.8 Time-resolved photoluminescence of aloin-Fe$_3$O$_4$@rGO and aloin-Fe$_3$O$_4$@rGO-TYR

Generally, the most definitive method to distinguish between static and dynamic quenching is the fluorescence lifetime. The non-variance of the lifetime (τ) values points to a static fluorescence quenching mechanism, while the substantial

tains 22.3% α-helix, 29.7% β-turn, 22.1% random coil, and 26.9% β-sheet. After the addition of Fe$_3$O$_4$@rGO, the conformation of TYR does not change significantly. With the addition of Fe$_3$O$_4$@rGO-aloin, the contents of α-helix, random coil, and β-turn show a downward trend (from 22.3% to 12.8%,
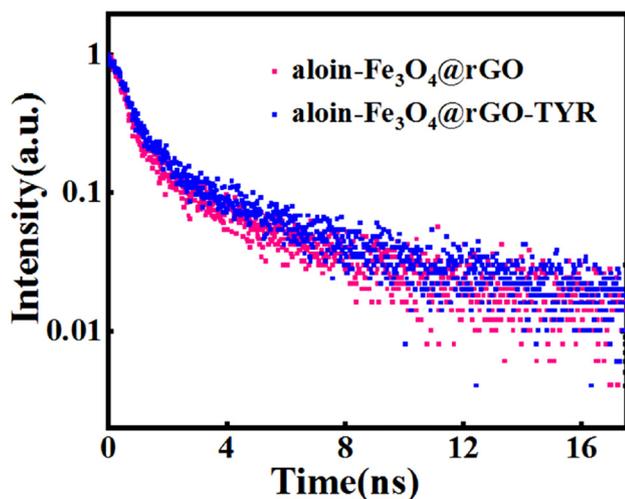
Fig. 9 Time-resolved fluorescence decays for Fe_3O_4@rGO-aloin without and in the presence of TYR. $C_{TYR} = 1.76 \times 10^{-7}$ mol L^{-1}, $C_{aloin} = 3.14 \times 10^{-5}$ mol L^{-1} and $C_{Fe_3O_4@rGO} = 7.31 \times 10^{-4}$ mg mL^{-1}.

Table 4 Time-resolved fluorescence parameters of aloin-Fe_3O_4@rGO and aloin-Fe_3O_4@rGO-TYR

Compounds	τ_1 (ns)	A_1%	τ_2 (ns)	A_2%	τ_{avg} (ns)	χ^2
Aloin-Fe_3O_4@rGO	0.62 ± 0.01	89.36	5.37 ± 0.52	12.11	3.19	1.3002
Aloin-Fe_3O_4@rGO-TYR	0.71 ± 0.01	86.45	5.44 ± 0.46	14.89	3.40	1.1874

A: relative amplitude. $\tau_{avg} = \dfrac{(A_1\tau_1{}^2 + A_2\tau_2{}^2)}{(A_1\tau_1 + A_2\tau_2)}$. χ^2: the fitting correlation coefficient.

decrease of the τ values reveals the appearance of a dynamic quenching process. The interaction of their lifetimes at excitation/emission wavelengths of 280/350 nm was investigated to gain insight into the quenching mechanism between TYR and Fe_3O_4@rGO-aloin (Fig. 9). Table 4 showed that the fluorescence lifetimes of aloin-Fe_3O_4@rGO ($\tau_1 = 0.62 \pm 0.01$ ns and $\tau_2 = 5.37 \pm 0.52$ ns, with relative percentages of 89.36% and 12.11%, respectively $\chi^2 = 1.3002$) and aloin-Fe_3O_4@rGO-TYR ($\tau_1 = 0.71 \pm 0.01$ ns and $\tau_2 = 5.44 \pm 0.46$ ns, with relative percentages of 86.45% and 14.89%, $\chi^2 = 1.1874$) were the same within the experimental error. This confirmed that the fluorescence quenching mechanism was a static process.[68]

4   Conclusions

Enzyme inhibition kinetics analysis and multispectral approaches were employed to investigate the interaction between Fe_3O_4@rGO-loaded aloin and TYR. Kinetic studies revealed that the IC_{50} value of aloin and Fe_3O_4@rGO-aloin on TYR were $(4.04 \pm 0.53) \times 10^{-5}$ mol L^{-1} and $(2.26 \pm 0.15) \times 10^{-5}$ mol L^{-1}, respectively. The experimental results clearly demon-

strated that the inhibitory effect of Fe_3O_4@rGO-aloin on TYR was more powerful than that of single aloin. From the Lineweaver–Burk diagram, it was evident that aloin and Fe_3O_4@rGO-aloin exhibit mixed inhibition and anticompetitive inhibition on TYR, respectively. The inhibition of TYR and the interaction mechanism of Fe_3O_4@rGO-loaded aloin were determined to be a static quenching process, primarily reliant on hydrophobic interaction. Aloin exhibited a moderate binding capacity to TYR, with a binding constant of approximately 10^4 L mol^{-1}. Furthermore, it was found that the combined ability of TYR and aloin was further enhanced by the addition of Fe_3O_4@rGO. The impact of Fe_3O_4@rGO-aloin on the microenvironment of TYR was demonstrated through synchronous fluorescence experiments. The impact of Fe_3O_4@rGO-aloin on the secondary structure of TYR was observed to be more pronounced compared to that of Fe_3O_4@rGO, as evidenced by 3D fluorescence, FT-IR and CD experiments. The findings of this study yield valuable insights for the design of functional magnetic reduced graphene oxide. Specifically, they offer a deeper understanding of the molecular-level interaction mechanism between Fe_3O_4@rGO-supported aloin and TYR. Such information is crucial for advancing research in this field and developing novel materials with enhanced properties.

Author contributions

Zhu Wang: data curation, investigation, software, formal analysis, and writing – original draft. Lu Chen: software, validation, formal analysis, writing – reviewing and editing, and visualization. Jing Yuan: investigation, data curation, validation, and formal analysis. Qiulan Zhang: conceptualization, methodology, supervision, funding acquisition, and writing – reviewing and editing. Yongnian Ni: visualization, writing – reviewing and editing, resources, and supervision.

Conflicts of interest

There are no conflicts of interest to declare.

Data availability

The authors confirm that the data supporting the findings of this study are available within the article. Additional data that support the findings of this study are available from the corresponding author, QLZ, upon reasonable request.

Acknowledgements

References

1 A. Ochiai, S. Tanaka, Y. Imai, H. Yoshida, T. Kanaoka, T. Tanaka and M. Taniguchi, New tyrosinase inhibitory decapeptide: Molecular insights into the role of tyrosine residues, *J. Biosci. Bioeng.*, 2016, **121**, 607–613, DOI: 10.1016/j.jbiosc.2015.10.010.

2 H. Maruyama, F. Kawakami, T. T. Lwin, M. Imai and F. Shamsa, Biochemical characterization of ferulic acid and caffeic Acid which effectively inhibit melanin synthesis via different mechanisms in B16 melanoma cells, *Biol. Pharm. Bull.*, 2018, **41**, 806–810, DOI: 10.1248/bpb.b17-00892.

3 Y. Wang, M. M. Hao, Y. Sun, L. F. Wang, H. Wang, Y. J. Zhang, H. Y. Li, P. W. Zhuang and Z. Yang, Synergistic promotion on tyrosinase inhibition by antioxidants, *Molecules*, 2018, **23**, 106, DOI: 10.3390/molecules23010106.

4 H. Y. Chen and Y. C. Yeh, Detection of tyrosine and monitoring tyrosinase activity using an enzyme cascade-triggered colorimetric reaction, *RSC Adv.*, 2020, **10**, 29745–29750, DOI: 10.1039/d0ra05581f.

5 G. X. Shi, Y. J. Feng and K. F. Tonissen, Development of a human tyrosinase activity inhibition assay using human melanoma cell lysate, *BioTechniques*, 2024, **76**(11), 547–551, DOI: 10.1080/07366205.2024.2441637.

6 D. S. Wavhal, D. Koszelewski, P. Kowalczyk, A. Brodzka and R. Ostaszewski, Synthesis, antimicrobial activity, and tyrosinase inhibition by multifunctional 3,4-dihydroxy-phenyl peptidomimetics, *Int. J. Mol. Sci.*, 2025, **26**(4), 1702, DOI: 10.3390/ijms26041702.

7 X. F. Min, L. Lu, X. T. Xu, Y. Wen and X. Zheng, Investigation on the inhibition mechanism and binding behavior of paeonol to tyrosinase and its anti-browning property by multi-spectroscopic and molecular docking methods, *Int. J. Biol. Macromol.*, 2023, **253**, 126962, DOI: 10.1016/j.ijbiomac.2023.126962.

8 Z. Y. Peng, Y. F. Li, L. J. Tan, L. Chen, Q. D. Shi, Q. H. Zeng, H. Q. Liu, J. J. Wang and Y. Zhao, Anti-tyrosinase, antioxidant and antibacterial activities of gallic acid-benzylidenehydrazine hybrids and their application in preservation of fresh-cut apples and shrimps, *Food Chem.*, 2022, **378**, 132127, DOI: 10.1016/j.foodchem.2022.132127.

9 M. He, M. Y. Fan, W. Yang, Z. Y. Peng and G. C. Wang, Novel kojic acid-1,2,4-triazine hybrids as anti-tyrosinase agents: Synthesis, biological evaluation, mode of action, and anti-browning studies, *Food Chem.*, 2023, **419**, 136047, DOI: 10.1016/j.foodchem.2023.136047.

10 G. C. Wang, M. He, Y. Huang and Z. Y. Peng, Synthesis and biological evaluation of new kojic acid-1,3,4-oxadiazole hybrids as tyrosinase inhibitors and their application in the anti-browning of fresh-cut mushrooms, *Food Chem.*, 2023, **409**, 135275, DOI: 10.1016/j.foodchem.2022.135275.

11 Z. Y. Peng, G. C. Wang, J. J. Wang and Y. Zhao, Anti-browning and antibacterial dual functions of novel hydroxypyranone-thiosemicarbazone derivatives as shrimp preservative agents: Synthesis, bio-evaluation, mechanism, and application, *Food Chem.*, 2023, **419**, 136106, DOI: 10.1016/j.foodchem.2023.136106.

12 M. Azimi, Z. Najafi, A. Bahmani, G. Chehardoli and A. Iraji, Synthesis and biological assessment of novel 4H-chromene-3-carbonitrile derivatives as tyrosinase inhibitors, *BMC Chem.*, 2024, **181**, 187, DOI: 10.1186/s13065-024-01305-0.

13 H. A. S. El-Nashar, M. I. G. El-Din, L. Hritcu and O. A. Eldahshan, Insights on the inhibitory power of flavonoids on tyrosinase activity: A survey from 2016 to 2021, *Molecules*, 2021, **26**, 7546, DOI: 10.3390/molecules26247546.

14 F. L. Liang, Inhibition mechanism investigation of quercetagetin as a potential tyrosinase inhibitor, *Front. Chem.*, 2024, **12**, 1411801, DOI: 10.3389/fchem.2024.1411801.

15 M. Y. Park, H. J. Kwon and M. K. Sung, Evaluation of aloin and aloe-emodin as anti-inflammatory agents in aloe by using murine macrophages, *Biosci., Biotechnol., Biochem.*, 2009, **73**, 828–832, DOI: 10.1271/bbb.80714.

16 G. Asamenew, D. Bisrat, A. Mazumder and K. Asres, In Vitro antimicrobial and antioxidant activities of anthrone and chromone from the latex of aloe harlana Reynolds, *Phytother. Res.*, 2011, **25**, 1756–1760, DOI: 10.1002/ptr.3482.

17 S. Kumar, D. P. Matharasi, S. Gopi, S. Sivakumar and S. Narasimhan, Synthesis of cytotoxic and antioxidant Schiff's base analogs of aloin, *J. Asian Nat. Prod. Res.*, 2010, **12**, 360–370, DOI: 10.1080/10286021003775327.

18 J. B. Xiao, S. Y. Chen, Y. Q. Chen and J. Q. Su, The potential health benefits of aloin from genus Aloe, *Phytother. Res.*, 2022, **36**, 873–890, DOI: 10.1002/ptr.7371.

19 Z. Wang, Z. You, L. Chen, Q. L. Zhang, X. Tuo and Y. N. Ni, Tyrosinase inhibition, molecular docking and molecular dynamics simulation studies of anthraquinone derivative from aloe vera as potential pigmentation dermatosis and anti-food browning agent, *Spectrosc. Lett.*, 2024, **57**, 452–468, DOI: 10.1080/00387010.2024.2373862.

20 F. Ameen, F. Alown, T. Dawoud, A. Sharaf, P. Sakayanathan and S. Alyahya, Versatility of copper-iron bimetallic nanoparticles fabricated using Hibiscus rosa-sinensis flower phytochemicals: various enzymes inhibition, antibiofilm effect, chromium reduction and dyes removal, *Environ. Geochem. Health*, 2024, **46**, 142, DOI: 10.1007/s10653-024-01918-3.

21 A. Angelopoulou, E. Voulgari, E. K. Diamanti, D. Gournis and K. Avgoustakis, Graphene oxide stabilized by PLA-PEG copolymers for the controlled delivery of paclitaxel, *Eur. J. Pharm. Biopharm.*, 2015, **93**, 18–26, DOI: 10.1016/j.ejpb.2015.03.022.

22 C. Zhang, T. Lu, J. G. Tao, G. Wan and H. X. Zhao, Co-delivery of paclitaxel and indocyanine green by PEGylated graphene oxide: a potential integrated nanoplatform for tumor theranostics, *RSC Adv.*, 2016, **6**, 15460–15468, DOI: 10.1039/c5ra25518j.

23 F. C. Jing, G. L. Li, Y. S. Wang, S. B. Zhu, R. D. Liu, J. He and J. D. Lei, Synthesis and characterization of folic acid-modified carboxymethyl chitosan-ursolic acid targeted

nano-drug carrier for the delivery of ursolic acid and 10-hydroxycamptothecin, *Polym. Adv. Technol.*, 2021, **32**, 343–354, DOI: **10.1002/pat.5090**.

24 S. Karimi and H. Namazi, Simple preparation of maltose-functionalized dendrimer/graphene quantum dots as a pH-sensitive biocompatible carrier for targeted delivery of doxorubicin, *Int. J. Biol. Macromol.*, 2020, **156**, 648–659, DOI: **10.1016/j.ijbiomac.2020.04.037**.

25 A. Rebekah, S. Sivaselvam, C. Viswanathan, D. Prabhu, R. Gautam and N. Ponpandian, Magnetic nanoparticle-decorated graphene oxide-chitosan composite as an efficient nanocarrier for protein delivery, *Colloids Surf., A*, 2021, **610**, 125913, DOI: **10.1016/j.colsurfa.2020.125913**.

26 A. A. Umar, M. F. A. Patah, F. Abnisa and W. M. A. W. Daud, Rational design of PEGylated magnetite grafted on graphene oxide with effective heating efficiency for magnetic hyperthermia application, *Colloids Surf., A*, 2021, **619**, 126545, DOI: **10.1016/j.colsurfa.2021.126545**.

27 M. Ashrafizadeh, A. Zarrabi, K. Hushmandi, F. Hashemi, E. R. Moghadam, M. Raei, M. Kalantari, S. Tavakol, R. Mohammadinejad, M. Najafi, F. R. Tay and P. Makvandi, Progress in natural compounds/siRNA Co-delivery employing nanovehicles for cancer therapy, *ACS Comb. Sci.*, 2020, **22**, 669–700, DOI: **10.1021/acscombsci.0c00099**.

28 W. Liu, X. Y. Zhang, L. Zhou, L. Shang and Z. Q. Su, Reduced graphene oxide (rGO) hybridized hydrogel as a near-infrared (NIR)/pH dual-responsive platform for combined chemo-photothermal therapy, *J. Colloid Interface Sci.*, 2019, **536**, 160–170, DOI: **10.1016/j.jcis.2018.10.050**.

29 R. Abbasi, J. M. Amjad, H. Nosrati, R. Mohammadkhani and H. Danafar, Synthesis and characterization of PEGylated iron and graphene oxide magnetic composite for curcumin delivery, *Appl. Organomet. Chem.*, 2020, **34**, e5825, DOI: **10.1002/aoc.5825**.

30 A. Alkhayal, A. Fathima, A. H. Alhasan and E. H. Alsharaeh, PEG coated Fe_3O_4/RGO nano-cube-like structures for cancer therapy via magnetic hyperthermia, *Nanomaterials*, 2024, **11**(9), 2398, DOI: **10.3390/nano11092398**.

31 H. Omar, Y. A. Alkurdi, A. Fathima and E. H. Alsharaeh, Investigation of the application of reduced graphene oxide–SPION quantum dots for magnetic hyperthermia, *Nanomaterials*, 2024, **14**(19), 1547, DOI: **10.1080/07366205.2024.2441637**.

32 C. Y. Qian, X. H. Liang, M. Wu and X. X. Zhang, Lightweight chain-typed magnetic Fe_3O_4@rGO composites with enhanced microwave-absorption properties, *Nanomaterials*, 2022, **12**, 3699, DOI: **10.3390/nano12203699**.

33 Y. H. Bi, Z. Y. Wang, Y. Q. Tian, H. R. Fan, S. Huang, Y. H. Lu and Z. Y. Jin, Highly efficient regioselective decanoylation of hyperoside using nanobiocatalyst of Fe_3O_4@PDA-thermomyces lanuginosus lipase: Insights of kinetics and stability evaluation, *Front. Bioeng. Biotechnol.*, 2020, **8**, 485, DOI: **10.3389/fbioe.2020.00485**.

34 Y. Q. Almulaiky, R. M. Ei-Shishtawy, M. Aldhahri, S. A. Mohamed, M. Afifi, W. H. Abdulaal and J. A. Mahyoub, Amidrazone modified acrylic fabric acti-

vated with cyanuric chloride: A novel and efficient support for horseradish peroxidase immobilization and phenol removal, *Int. J. Biol. Macromol.*, 2019, **140**, 949–958, DOI: **10.1016/j.ijbiomac.2019.08.179**.

35 M. H. Fan, G. W. Zhang, X. Hu, X. M. Xu and D. M. Gong, Quercetin as a tyrosinase inhibitor: Inhibitory activity, conformational change and mechanism, *Food Res Int.*, 2017, **100**, 226–233, DOI: **10.1016/j.foodres.2017.07.010**.

36 H. F. Ding, X. Q. Wu, J. H. Pan, X. Hu, D. M. Gong and G. W. Zhang, New Insights into the Inhibition Mechanism of Betulinic Acid on α-Glucosidase, *J. Agric. Food Chem.*, 2018, **66**, 7065–7075, DOI: **10.1021/acs.jafc.8b02992**.

37 Q. Yu and L. P. Fan, Understanding the combined effect and inhibition mechanism of 4-hydroxycinnamic acid and ferulic acid as tyrosinase inhibitors, *Food Chem.*, 2021, **352**, 129369, DOI: **10.1016/j.foodchem.2021.129369**.

38 X. Song, X. Hu, Y. Zhang, J. H. Pan, D. M. Gong and G. W. Zhang, Inhibitory mechanism of epicatechin gallate on tyrosinase: inhibitory interaction, conformational change and computational simulation, *Food Funct.*, 2020, **11**, 4892–4902, DOI: **10.1039/d0fo00003e**.

39 N. Zare-Feizabadi, Z. Amiri-Tehranizadeh, A. Sharifi-Rad, P. Mokaberi, N. Nosrati, F. Hashemzadeh, H. R. Rahimi, M. R. Saberi and J. Chamani, Determining the interaction behavior of calf thymus DNA with anastrozole in the presence of histone H1: spectroscopies and cell viability of MCF-7 Cell line investigations, *DNA Cell Biol.*, 2021, **40**, 1039–1051, DOI: **10.1089/dna.2021.0052**.

40 D. Wu, X. Hu, Z. Y. Cai, J. Zhang, F. Geng and H. Li, Binding behavior and antioxidant study of spice extract piperine with respect to meat myoglobin, *Food Funct.*, 2023, **14**, 6422–6431, DOI: **10.1039/d3fo00617d**.

41 W. Guan, J. Cheng, D. J. McClements, Z. C. Tu, J. Chen and D. Ma, Impact of 2, 4-di-tert-butylphenol on pancreatic lipase activity in emulsions: Multispectral, molecular docking, and in vitro digestion analysis, *Food Chem.*, 2025, **470**, 142730, DOI: **10.1016/j.foodchem.2024.142730**.

42 J. M. Wu, Z. M. Ye, W. X. Liu, Z. F. Liu and J. Chen, The effect of GO loading on electromagnetic wave absorption properties of Fe_3O_4/reduced graphene oxide hybrids, *Ceram. Int.*, 2017, **43**, 13146–13153, DOI: **10.1016/j.ceramint.2017.07.007**.

43 D. Verma, M. Okhawilai, N. Senthilkumar, K. Subramani, A. Ncharoensakdi, G. G. Raja and H. Uyama, Augmentin loaded functionalized halloysite nanotubes: A sustainable emerging nanocarriers for biomedical applications, *Environ. Res.*, 2024, **242**, 117811, DOI: **10.1016/j.envres.2023.117811**.

44 H. Nabipour, F. Aliakbari, K. Volkening, M. J. Strong and S. Rohani, Development of metal-organic framework biocomposites from chitosan as drug delivery vehicles: In vitro evaluation on HeLa and SH-SY5Y cell lines, *Int. J. Biol. Macromol.*, 2025, **291**, 138878, DOI: **10.1016/j.ijbiomac.2024.138878**.

45 Y. J. Feng, X. Zhang, Y. Zhong, S. Q. Yang and J. Wang, Flexible spiral-like multilayer composite with Fe_3O_4@rGO/

waterborne polyurethane-Ni@polyimide for enhancing electromagnetic shielding, *Colloids Surf., A*, 2023, **662**, 131006, DOI: **10.1016/j.colsurfa.2023.131006**.

46 A. J. Khan, A. Khan, M. S. Javed, M. Arshad, S. Asim, M. Khalid, S. H. Siyal, S. Hussain, M. Hanif and Z. W. Liu, Surface assembly of Fe_3O_4 nanodiscs embedded in reduced graphene oxide as a high-performance negative electrode for supercapacitors, *Ceram. Interfaces*, 2020, **46**, 19499–19505, DOI: **10.1016/j.ceramint.2020.04.303**.

47 Y. L. Yang, C. S. Wang, J. L. Zhou, B. W. Li, C. Liu and A. H. Shen, Effects of Fe_2O_3-[BOx] reaction on sodium borosilicate glass structure doping with nano to macro sized α-Fe_2O_3 particles, *J. Mol. Struct.*, 2024, **1299**, 137201, DOI: **10.1016/j.molstruc.2023.137201**.

48 H. N. Wang, Z. Y. Li, S. T. Lu, C. Y. Li, W. C. Zhao, Y. L. Zhao, S. L. Yu, T. Wang and T. D. Sun, Nano micelles of cellulose -graft -poly (L -lactic acid) anchored with epithelial cell adhesion antibody for enhanced drug loading and anti -tumor effect, *Mater. Today Commun.*, 2020, **22**, 100764, DOI: **10.1016/j.mtcomm.2019.100764**.

49 S. Y. Yu, M. He, Y. H. Zhai, Z. K. Xie, S. Xu, S. X. Yu, H. F. Xiao and Y. D. Song, Inhibitory activity and mechanism of trilobatin on tyrosinase: kinetics, interaction mechanism and molecular docking, *Food Funct.*, 2021, **12**, 2569–2579, DOI: **10.1039/d0fo03264f**.

50 Q. Q. Chen, W. Y. Tao, J. F. Wang, J. R. Li, M. Y. Zheng, Y. Y. Liu, S. M. Lu and Z. X. Fang, Inhibitive mechanism of loquat flower isolate on tyrosinase activity and melanin synthesis in mouse melanoma B16 cells, *Biomolecules*, 2024, **14**(8), 895, DOI: **10.3390/biom14080895**.

51 J. F. Zhang, S. S. Li, X. B. Liu and L. J. Sun, Inconsistency between polyphenol-enzyme binding interactions and enzyme inhibition: Galloyl moiety decreases amyloglucosidase inhibition of catechins, *Food Res. Int.*, 2023, **163**, 112155, DOI: **10.1016/j.foodres.2022.112155**.

52 N. Mumtaz, M. Imran, A. Javaid, S. Latif, N. Hussain and L. Mitu, Nanomaterials for targeted drug delivery through skin to treat various diseases: recent trends and future perspective, *J. Chem.*, 2023, **2023**, 3861758, DOI: **10.1155/2023/3861758**.

53 Y. Y. Ma, D. G. Zhao, R. Q. Zhang, X. He, B. Q. Li, X. Z. Zhang, Z. J. Wang and K. Zhang, Identification of bioactive compounds that contribute to the α-glucosidase inhibitory activity of rosemary, *Food Funct.*, 2020, **11**, 1692–1701, DOI: **10.1039/c9fo02448d**.

54 L. L. Liu, J. D. Li, L. L. Zhang, S. D. Wei, Z. Y. Qin, D. D. Liang, B. M. Ding, H. Chen and W. Song, Conformational changes of tyrosinase caused by pentagalloylglucose binding: Implications for inhibitory effect and underlying mechanism, *Food Res. Int.*, 2022, **157**, 111312, DOI: **10.1016/j.foodres.2022.111312**.

55 X. G. Zhang, C. C. Hao, Z. Z. Nan and R. G. Sun, Fluorescence quenching study on the interaction of Lycium barbarum polysaccharide with bovine serum albumin, *Appl. Phys. Express*, 2019, **12**, 092007, DOI: **10.7567/1882-0786/ab37ab**.

56 J. T. Pang, Y. L. Song, L. J. Chen, Y. L. Li, F. Geng, N. Gan, X. H. Wang, Q. L. Wang, T. T. Zeng and D. Wu, Multispectral methods combined with computer simulation to explore the binding mechanism of the azo pigment allure red to hemoglobin and myoglobin, *LWT – Food Sci. Technol.*, 2025, **221**, 117603, DOI: **10.1016/j.lwt.2025.117603**.

57 L. J. Yang, G. J. Nan, X. X. Meng, L. N. Zhang, N. Song, Y. Liu, Z. Z. Liu, Y. Wang and G. D. Yang, Study on the interaction between lovastatin and three digestive enzymes and the effect of naringin and vitamin C on it by spectroscopy and docking methods, *Int. J. Biol. Macromol.*, 2020, **155**, 1440–1449, DOI: **10.1016/j.ijbiomac.2019.11.120**.

58 C. Dufour and O. Dangles, Flavonoid-serum albumin complexation: determination of binding constants and binding sites by fluorescence spectroscopy, *BBA, Gen. Subj.*, 2005, **1721**, 164–173, DOI: **10.1016/j.bbagen.2004.10.013**.

59 M. He, Y. H. Zhai, Y. Q. Zhang, S. Xu, S. X. Yu, Y. X. Wei, H. F. Xiao and Y. D. Song, Inhibition of α-glucosidase by trilobatin and its mechanism: kinetics, interaction mechanism and molecular docking, *Food Funct.*, 2021, **12**, 2569–2579, DOI: **10.1039/d0fo03264f**.

60 A. Mahdavi, N. Mohammadsadeghi, F. Mohammadi, F. Saadati and S. Nikfard, Evaluation of inhibitory effects of some novel phenolic derivatives on the mushroom tyrosinase activity: Insights from spectroscopic analyses, molecular docking and in vitro assays, *Food Chem.*, 2022, **387**, 132938, DOI: **10.1016/j.foodchem.2022.132938**.

61 M. Fatima, F. Nabi, R. H. Khan and A. Naeem, Investigating the binding interaction of quinoline yellow with bovine serum albumin and anti-amyloidogenic behavior of ferulic acid on QY-induced BSA fibrils, *Spectrochim. Acta, Part A*, 2024, **313**, 124076, DOI: **10.1016/j.saa.2024.124076**.

62 C. F. Bi, R. D. Jiang, X. W. He, L. X. Chen and Y. K. Zhang, Synthesis of a hydrophilic maltose functionalized Au NP/PDA/Fe_3O_4-rGO magnetic nanocomposite for the highly specific enrichment of glycopeptides, *RSC Adv.*, 2015, **5**, 59408–59416, DOI: **10.1039/c5ra06911d**.

63 D. Ray, B. K. Paul and N. Guchhait, Effect of biological confinement on the photophysics and dynamics of a proton-transfer phototautomer: an exploration of excitation and emission wavelength-dependent photophysics of the protein-bound drug, *Phys. Chem. Chem. Phys.*, 2012, **14**, 12182–12192, DOI: **10.1039/c2cp41292f**.

64 Q. F. Chen, C. Shang, M. Q. Han, C. Chen, W. K. Tang and W. B. Liu, Inhibitory mechanism of scutellarein on tyrosinase by kinetics, spectroscopy and molecular simulation, *Spectrochim. Acta, Part A*, 2023, **296**, 122644, DOI: **10.1016/j.saa.2023.122644**.

65 A. J. Rahman, L. Kaur, M. Pathak, A. Singh, P. Verma, R. Singhal, V. Kumar and H. Ojha, Spectroscopic studies of binding interactions of 2-chloroethylphenyl sulphide with bovine serum albumin, *J. Mol. Liq.*, 2021, **340**, 117144, DOI: **10.1016/j.molliq.2021.117144**.

66 J. Chen, Z. W. Zhang, H. H. Li and H. J. Tang, Exploring the effect of a series of flavonoids on

tyrosinase using integrated enzyme kinetics, multispectroscopic, and molecular modelling analyses, *Int. J. Biol. Macromol.*, 2023, **252**, 126451, DOI: **10.1016/j.ijbiomac.2023.126451**.

67 H. J. Zeng, D. Q. Sun, S. H. Chu, J. J. Zhang, G. Z. Hu and R. Yang, Inhibitory effects of four anthraquinones on tyrosinase activity: Insight from spectroscopic analysis and molecular docking, *Int. J. Biol. Macromol.*, 2020, **160**, 153–163, DOI: **10.1016/j.ijbiomac.2020.05.193**.

68 S. Y. Niu, X. Liu, J. Liu, B. Yang, X. Wang, L. Q. Niu and S. Y. Bi, High efficiency methods for the determination of dinotefuran and imidacloprid by fluorescence spectrometry using whey protein as sensor, *J. Mol. Struct.*, 2025, **1329**, 141437, DOI: **10.1016/j.molstruc.2025.141437**.